Nanoscale

Accepted Manuscript

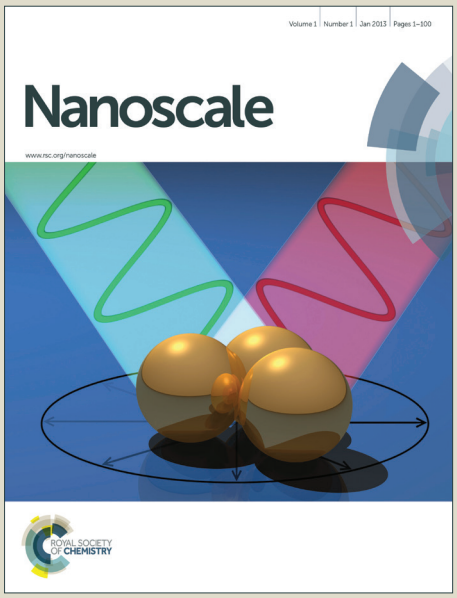

Nanoscale

PAPER

In vivo 808nm Image-Guided Photodynamic Therapy based on Upconversion Theranostic Nanoplatform

Received 00th January 20xx,
Accepted 00th January 20xx

DOI: 10.1039/x0xx00000x

www.rsc.org/

Xiaomin Liu,[a] Ivo Que,[b] Xianggui Kong,[a]* Youlin Zhang,[a] Langping Tu,[a] Yulei Chang,[a] Tong Tong Wang,[a] Alan Chan,[b,d] Clemens W. G. M. Löwik,[b] Hong Zhang[a,c]*

A new strategy for efficient *in vivo* image-guided photodynamic therapy (PDT) has been demonstrated utilizing ligand-exchange constructed upconversion-C_{60} nanophotosensitizer. This theranostic platform is superior over the current reported nanophotosensitizers on (i) directly bonding photosensitizer C_{60} to the surface of upconversion nanoparticles (UCNPs) by a smart ligand-exchange strategy, which greatly shortened the energy transfer distance and enhanced the $^1O_2$ production, resulting in improvement of the therapeutic effect; (ii) realizing *in vivo* NIR 808nm image-guided PDT with both the excitation (980nm) and emission (808nm) light fall in the biological window of tissues, which minimized auto-fluorescence, reduced light scatting and improved the imaging contrast and depth, thus guaranteed noninvasive diagnostic accuracy. *In vivo* and *ex vivo* tests demonstrated its favorable bio-distribution, tumor-selectivity and high therapeutic efficacy. Owing to the effective ligand exchange strategy and the excellent intrinsic photophysical properties of C_{60}, $^1O_2$ production yield was improved to such that a low 980 nm irradiation dosage (351 J/cm^2) and short treatment time (15 min) were sufficient to perform NIR (980nm) to NIR (808nm) image-guided PDT. Our work enriches the UCNPs-based nanophotosensitizers and highlights their potential in future NIR image-guided noninvasive deep cancer therapy.

1. Introduction

Photodynamic therapy (PDT) is a non-invasive medical therapeutic technology using photosensitizers (PS) and light irradiation to treat cancers.[1,2] However, current photosensitizers are mostly activated by visible (VIS) light, which restricts PDT to superficial cancers due to light absorption by tissue.[3,4] In recent years, this obstacle has been improved by lanthanide ion (Ln^{3+}, such as Er^{3+}, Tm^{3+}, Ho^{3+})-doped upconversion nanoparticles (UCNPs), which are considering as a new generation of multimodal bio-probes, and have attracted great interest in a variety of biological applications.[5-10] The reported luminescence UCNPs based nanophotosensitizer (NPS),[11-22] which can be triggered with NIR light (~ 980 nm) locating in the biological window of tissues (700-1300nm), has made PDT capable to treat deeper lesions that could not realized by visible light. On top of that, these UCNP-based NPS can enhance greatly the quality of imaging because of the significant reduction of the autofluorescence of background due to the near infrared (NIR) excitation.[23,24]

Up to now, there are three general methods to incorporate PS to UCNP, including physical adsorption,[11,13,17] physical encapsulation,[12,14-16] and covalent conjugation.[18,19] Physical adsorption method was at initial stage popular, which however inevitably suffered from low loading capacity and untimely release of PS from UCNP during blood circulation.[17] Afterwards, physical encapsulation, which could load PS on UCNPs through hydrophobic interaction, was introduced and demonstrated to possess higher drug loading capacity.[15] However, the high loading capacity of PS did not result in a desired PDT efficiency because of the increased energy transfer distance in such physical encapsulation.[14] Lately, the developed covalent conjugation of PS to UCNP have been proved of being able to effectively suppress the leaking of PS from UCNPs.[18] However, the surface of the UCNPs should be firstly functionalized with amino or carboxyl group before covalent conjugation, which still impeded the energy transfer distance.[19] Recently, the covalent conjugation and physical absorption of PS to UCNP were combined to maximize the PDT efficacy.[20] In a word, searching for a much more effective conjoint strategy, which could satisfy high fluorescence resonance energy transfer (FRET) efficiency, has always being a challenge.

Among the aforementioned UCNPs-based NPSs, the upconverted visible lights were always applied for imaging, which did not fall into the most favorable area of the biological window (700-1300nm) and astricted the signal-to-noise ratio. In addition, in all these cases, the $NaYF_4$: Yb^{3+}, Er^{3+} UCNP was the only model for donor, the limited spectral overlap between Er^{3+} and the acceptors restricted the $^1O_2$ production yield.[11-22] Typically, most of the currently used

a. State Key Laboratory of Luminescence and Applications. Changchun Institute of Optics, Fine Mechanics and Physics, Chinese Academy of Sciences. 130033, Changchun, Jilin, China.
b. Experimental Molecular Imaging, Department of Radiology, Leiden University Medical Center, 2333 ZA Leiden, The Netherlands.
c. Van't Hoff Institute for Molecular Sciences. University of Amsterdam, Science Park 904, 1098 XH Amsterdam, The Netherlands.
d. Percuros B.V., Building Zuidhorst, Drienerlolaan 5, 7522 NB Enschede, The Netherlands.

Electronic Supplementary Information (ESI) available: [details of any supplementary information available should be included here]. See DOI: 10.1039/x0xx00000x

photosensitizers are organic dyes, with the drawback of negative side effects, photobleaching and limited $^1O_2$ production. [19]

Given this, we have in this work, demonstrated a realizable *in vivo* NIR (980nm) to NIR (808nm) image-guided PDT utilizing a highly efficient FRET upconversion-C_{60} nanoplatform constructed via ligand-exchange approach. Superior to traditional PS, fullerene derivatives possess broad absorption spectra, are lack of dark toxicity[25] and "hard" enough to endure relatively high density photoexcitation[26], and most of all, have nearly 1.0 $^1O_2$ quantum yield.[27,28] In so-designed UCNPs-C_{60}MA NPS, high $^1O_2$ production yield was actualized by multiplexed FRET in which multicolor Er^{3+} and Tm^{3+} separately doping UCNPs were the energy donors and C_{60}MA the acceptor. Upon 980 nm CW light excitation, upconversion luminescence appeared simultaneously around 360, 407, 450, 475, 540, 650, 696 and 808 nm. All the emissions except 808 nm could transfer the energy to C_{60}MA to triggered PDT. Meanwhile, the 808 nm NIR emission was applied for high contrast NIR luminescence imaging (Scheme 1). It should be emphasized that both the excitation and emission were located in the best area of the optical window, which minimized auto-fluorescence and reduced light scatting, thus guaranteed the noninvasive detection sensitivity. Initially, we have followed the covalent way[19] to construct the UCNPs-C_{60}MA conjugate. However, the multi-step synthesis and the relative long distance between UCNPs and C_{60}MA result in relative poor $^1O_2$ production yield[34]. To improve this situation, a ligand exchange strategy, by which C_{60}MA could simply and directly bond to the surface of UCNPs, was adopted to greatly shorten the energy transfer distance (see Fig. S2). Owing to the ligand exchange assembly and excellent intrinsic photophysical properties of C_{60}, $^1O_2$ production yield was improved to such that a low 980 nm irradiation power density of 0.39 W/cm^2, which is far below the tolerance for human skin exposure to 980 nm light (0.72 W/cm^2),[17] and a short treatment time (15 min) were sufficient to perform NIR image-guided PDT. *In vivo* 980nm NIR-triggered 808 nm NIR imaging and PDT evidenced the high detection sensitivity, favorable bio-distribution, tumor-selectivity and distinct therapeutic efficacy with tumor inhibition ratio up to 78.5%. This effort offers an efficient nanophotosensitizer suitable for high quality NIR to NIR image-guided therapy of cancer. Furthermore, this ligand-exchange concept can be extended to any other systems based on FRET for improving their performances.

2. Materials and Methods

2.1 Materials

$YCl_3 \bullet xH_2O$ (99.9%), $YbCl_3 \bullet xH_2O$ (99.9%), $ErCl_3 \bullet xH_2O$ (99.9%), $TmCl_3 \bullet xH_2O$ (99.9%), NaOH (98%), NH_4F (98%), 1-octadecene (90%), Oleylamine (OM), Folic acid were purchased from Sigma-Aldrich. Fluoresceinyl cypridina luciferin analogue (FCLA) was purchased from Tokyo Kasel Kogyo Co. Tokyo, Japan. All chemicals were used as received without further purification. Core, Core-shell nanoparticles and Monomalonic Fullerene (C_{60}MA) were synthesized according to our previous work.[34]

2.2. Synthesis of PEG-b-PCL

ε-Caprolactone (ε-CL) monomer was distilled from calcium hydride and DL-lactide monomer was purified three times by recrystallization in toluene before use. Monomethoxy poly(ethyle glycol) (mPEG-OH, Mw=5000g/mol) was pretreated by azeotropi distillation in toluene to remove water. mPEG-OH (2g) and ε-C monomers (2.8g) were dissolved in anhydrous dichlorometha (100mL). Hydrochloric acid (2M in diethyl ether) (0.2mL) was adde as a catalyst and the reaction proceeded at 25°C under nitrogen for 24 h. mPEG-b-PCL block copolymers were precipitated into ice-co hexane, filtered, and vacuum-dried.

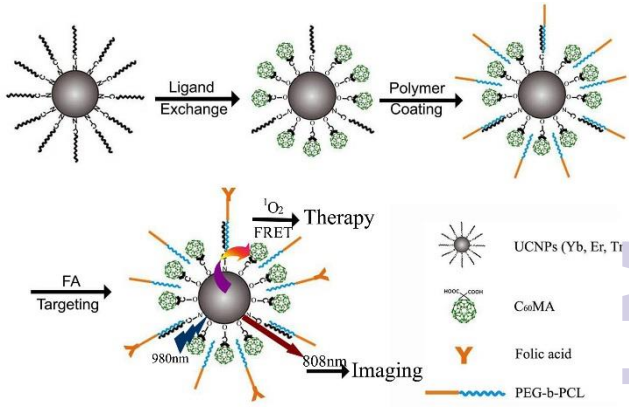

Scheme 1. The construction and operating principle of the UCNPs-C_{60}MA nanophotosensitizer.

2.3. Ligand exchange assembly and surface functionalization

The hydrophobic UCNPs solution (~5mg, purified and dispersed i 2mL of cyclohexane) was mixed with the different amounts of C_{60}MA Tetrahydrofuran (THF) solution and stirred vigorously ove 24 h at 30 °C. UCNPs-C_{60}MA conjugates were then centrifuged and washed with acetone to remove any unreacted C_{60}MA. Th obtained nanocomposites were redispersed in THF. To surface coa UCNPs-C_{60}MA with PEG-b-PCL molecules, 4mg PEG-b-PCL an 0.5mg UCNPs-C_{60}MA nanocomposites were dissolved in 4mL THF. The above solution was slowly added into 10mL of deionized w er under sonication and stirred for 12h at room temperature to remove THF. UCNPs-C_{60}MA conjugates were then centrifuged and washed with water to remove any unreacted PEG-b-PCL.

2.4. C_{60}MA loading capacity

The concentration of C_{60}MA was calculated by Beer-Lambert la $A = \varepsilon bc$, where A represents the absorption value; ε is the extinctio coefficient of C_{60}MA which is determined as 745 $l \cdot mol^{-1} \cdot cm^{-1}$ at 51 nm in THF solution; b equals to 1 cm; c is the concentration. Th absorption value should cover the range from 0.3 to 0.6. UCNPs o 0.5 mg/ml were mixed with various amounts of C_{60}MA. Afte removing free C_{60}MA by washing, a certain amount of UCNP C_{60}MA was diluted by THF, UV-VIS absorption spectra of UCNP C_{60}MA NPs were recorded. UV-VIS absorption spectra of UCNP were also measured as background in the same way. The C_{60}MA loading capacity = [amount of C_{60}MA in the UCNPs (g)] / [amount o UCNPs-C_{60}MA (g)] ×100.

2.5. In vitro Cell Imaging and PDT

0.05 mg Folic acid was dissolved in N,N-Dimethylformamide (DMF) and mixed with 0.5mg of PEG-b-PCL functionalized UCNPs-C_{60}MA, and stirred for 24 h in the dark. The resulting nanoconjugates were collected by centrifugation, washed with water three times, redispersed in 5 mL of phosphate buffer, and stored in the dark at 4 °C for further application. The concentration of folic acid was also calculated by Beer-Lambert law $A = \varepsilon bc$, where ε is the extinction coefficient of folic acid which is determinted as 788 $l \cdot mol^{-1} \cdot cm^{-1}$ at 360nm in DMF/water solution. Considering the big overlap between the absorption of C_{60}MA and folic acid, we adopted the subtractive absorption process. 1 ml PEG-b-PCL functionalized UCNPs-C_{60}MA (0.6mg/ml) was mixed with certain amount of folic acid DMF solution (0.1 mg/ml). Before mixing, the absorption spectrum of the added folic acid solution was determined. After centrifugation, the absorption spectrum of the elute was also measured. Based on the subtractive absorption value, we can evaluate the amount of folic acid attached to UCNPS-C_{60}MA NPs. The folic acid loading capacity = [amount of folic acid in the UCNPS-C_{60}MA (g)] / [amount UCNPS-C_{60}MA (g)] ×100. It turns out that the loading capacity was 5.1% (w/w). The details of the cell imaging and PDT were carried out according to our previously work[34] with the difference that 0.39W/cm^2 was set for the 980nm laser (diode laser, NL-PPS50).

2.6. In vivo imaging

All procedures were approved by the Leiden University animal experimental committee, performed in accordance with the national legislation of the Netherlands and in compliance with the 'Code of Practice Use of Laboratory Animals in Cancer Research' (Inspectie W&V, July 1999). Athymic mice (BALB/c nu/nu 6 weeks old) were acquired from Charles River (Charles River, L'Arbresle, France), housed in individually ventilated cages, and food and water was provided ad libitum. 3×10^6 Hepal-6 tumors cells were subcutaneously injected in nude mousee and after 2 weeks of tumor growth, V= 125mm^3, Photon intensity = 10^6/sec/cm^2, 100µL (3mg/mL) of UCNPs-C_{60}MA was administered iv. After 2, 24, 48 and 72 hours post injection of UNCP, mouse was measured in the IVIS Spectrum (CaliperLS, Hopkinton) The interior platform of the animal housing unit of the IVIS Spectrum imager was adapted to hold a clamp which was attached onto a 980nm laser head. The power supply for the laser was placed outside of the imager but connected by wires inserted through the door entrance of the imager. Organs (hart, liver, spleen, kidney, tumor and bladder) were *ex-vivo* measured 72 hours post injection.

2.7. In vivo PDT treatment

Female C57/6J mice (20g, 6-8 weeks old) used in this study were purchased from the First Bethune Hospital, University of Jilin. All experiments were carried out in compliance with the animal management. The Hepa1-6 tumor model was established by subcutaneously inoculating Hepa1-6 cells (3×10^6) into the upper axillary fossa in the mice (n=6). 100µL saline or UCNPs-C_{60}MA (3mg/ml) was intra-tumorally injected into each Hepa1-6 tumor-bearing mouse. The mice were randomly assigned into four groups treated with different injections, as follows: (1) group 1:subcutaneous injection of the saline (the control group, n=6); (2) group 2: subcutaneous injection of the saline with NIR light irradiation (n=6); (3) group 3 :subcutaneous injection of the UCNPs-C_{60}MA (n=6); (4) group 4:subcutaneous injection of the UCNPs-C_{60}MA with NIR light irradiation (n=6). The tumors were irradiated with a 980 nm laser light (0.39 W cm^{-2}) for 15 min. To avoid any tissue damage by heating, the laser treatment was done with 3 min interval for every 3min of light exposure. After treatment, the tumor volume was calculated as length× (width)^2×1/2 with a caliper over 2 weeks. The body weight of each mouse was monitored every other day over 2 weeks. Inhibition ratio = $(V_c - V_t)/V_c \times 100\%$, V_c and V_t represent the average tumor volume for the control group and treatment group, respectively.

2.8. Statistical analysis.

The differences were determined using the Student's t test where differences were considered ($p < 0.05$). All data are expressed as mean ± standard error of the mean.

3. Results and Discussion

3.1. Comparison of C60 with other photosensitizers

Singlet oxygen production efficiency is the most important factor for PDT. The ideal drug for PDT should have a high quantum yield of $^1O_2$, absorption in NIR and/or far IR range, and low toxicity without light irradiation. The most employed photosensitizers for PDT studies are organic dyes, such as methylene blue (MB), rose bengal (RB), or eosin (EO), which are well known as singlet oxygen generation.[29] The drawback of them are negative side effects (like anaphylactic reaction of the skin), photobleaching and limited $^1O_2$ production. Lately, fullerene derivatives have been investigated as novel and much more efficient photosensitizers. Such molecules consist of 60 carbon molecules arranged in a characteristic soccer ball shape. The symmetry and conjugated π-bond system of C_{60} result in a number of unique properties, e.g. broad absorption, photostability.[30,31] Furthermore, it was evidenced that the singlet oxygen yields of MB, RB, EO and C_{60} are 0.1713, 0.0982, 0.0394 and 0.4729 in benzene-methanol solutions, respectively,[29] indicating that the efficiency of singlet oxygen production by C_{60} is higher than the most frequently used sensitizers in photodynamic studies. For example it is approximately 12-fold higher than that of EO, and several-fold higher than those of RB and MB. This is mainly because that C_{60} possesses a high degree of symmetry (I_h), transitions between the ground state and the singlet state are strongly forbidden.[29] This forbiddenness determines that intersystem crossing (ISC) is a dominant process. The triplet state of C_{60} is formed in high yield and the triplet life time is very long (40±4µs).[32] Efficient generation of singlet oxygen can thus be obtained by energy transfer from the highly populated C_{60} triplet state to the dioxygen ground state.

3.2. Ligand-exchange assembly and characterization of nanophotosensitizer

For energy transfer based PDT, high energy transfer efficiency is essential to achieve high $^1O_2$ production. For this purpose, a ligand exchange strategy was applied to construct the UCNPs-based NPs

order to shorten the energy transfer distance. Matching the broad absorption spectrum of fullerene, oleylamine-coated $NaYF_4$: Yb^{3+}, Er^{3+}/ $NaYF_4$: Yb^{3+}, Tm^{3+} multicolor UCNPs were constructed (see experimental section). From the TEM images it could be seen that the UCNPs distribute with diameter of 34±5.8 nm (Fig. 1a, Fig. S1). In oleylamine-coated NPs, the amino groups coordinate to the lanthanide ions (Ln^{3+}) on the surface of the NPs. Considering that the coordination ability of Ln^{3+} - O is stronger than that of Ln^{3+} - N, the carboxyl groups of C_{60}MA could easily replace oleylamine and coordinate to Ln^{3+} (Fig. S2a). Therefore, Ligand exchange involved an exchange reaction between the amino group of the ligands on the UCNPs and the carboxyl group of C_{60}MA. The ligand exchange process did not effect on the size and morphology of UCNPs (Fig. 1b). To increase the dispersity of nanocomposites in biology relevant media, Poly (ethylene glycol)-block-Poly (caprolactone) (PEG-b-PCL),[33] was used to stabilize the nanocomposites in various biological mediums (Fig. S3). Hydrodynamic diameter distributions of the UCNPs before and after ligand exchange, and further after polymer coating were measured centered at about 34 nm, 43 nm and 92 nm, respectively, indicating successful surface functionalization (Fig. S4). FTIR absorption spectra evidenced the success in ligand exchange between UCNPs and C_{60}MA (Fig. S5). The changes in the carbonyl region (υ=1650-1710cm^{-1}) were taken as indicative of bond formation between the C_{60}MA carboxylic acid group and the inorganic nanoparticles. The binding of C_{60}MA was also confirmed by the fact that dark brown precipitates and nearly colorless supernatants were observed after centrifugation, while no precipitates or color change was noticed in the bare C_{60}MA sample (inset in Fig. S5).

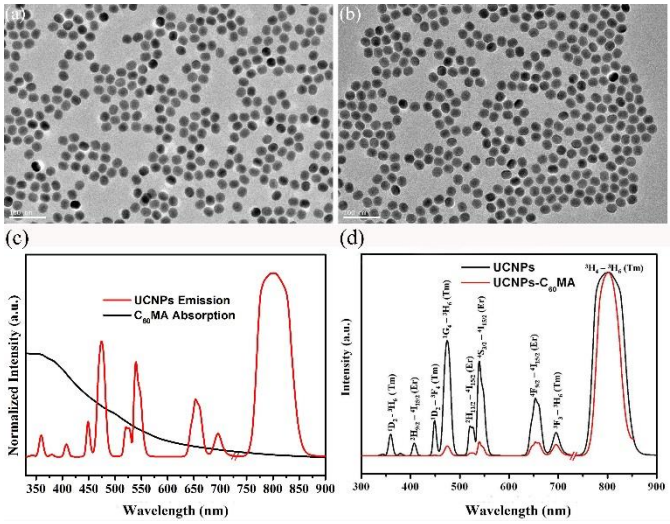

Fig. 1. (a) TEM images of $NaYF_4$: Yb^{3+}, Er^{3+}/$NaYF_4$: Yb^{3+}, Tm^{3+} core/shell UCNPs. (b) TEM images of ligand exchange assembled UCNPs-C_{60}MA nanophotosensitizer. (c) Spectral overlap between the emission of the donor UCNPs (red) and the absorption of the acceptor C_{60}MA (black). (d) UCL spectra of UCNPs and UCNPs-C_{60}MA nanophotosensitizer (normalized by the intensity at 808nm, the range from 300 to 730 nm was magnified by a factor of 10).

The payload and stability of the UCNP-C_{60}MA NPS were then studied in detail (Fig. S6). In the C_{60}MA loading process, UCNPs was firstly ligand-exchanged with excess C_{60}MA because the ligand-exchange is a dynamic process and then surface coated with PEG-b-PCL. UV-VIS absorption spectra of UCNP-C_{60}MA NPS were recorded (see experimental section). It was found that the C_{60}MA load capacity increased with the amount of C_{60}MA, and saturated at 22.5 (w/w) when the amount of C_{60}MA was 0.14 mg (Fig. S6a), which was approximately twice as high as that of the covalent assembled UCNP-C_{60}MA NPS (10.5% w/w) (see Fig. S2b).[34] The release of C_{60}MA in UCNP-C_{60}MA NPS was measured in pH 7.4 PBS, showing a slow releasing rate with 2.5% of C_{60}MA detached from UCNPs after 72h (Fig. S6b), which is less than that of the covalent assembled UCNP-C_{60}MA NPS (11.2%). The stability was also performed in bovine serum, demonstrating that only 4.8 wt% of C_{60}MA released from the ligand exchange constructed UCNP-C_{60}MA NPS after 72 h (Fig. S6c). The good stability of the UCNP-C_{60}MA NPS facilitated their application in biomedicine.

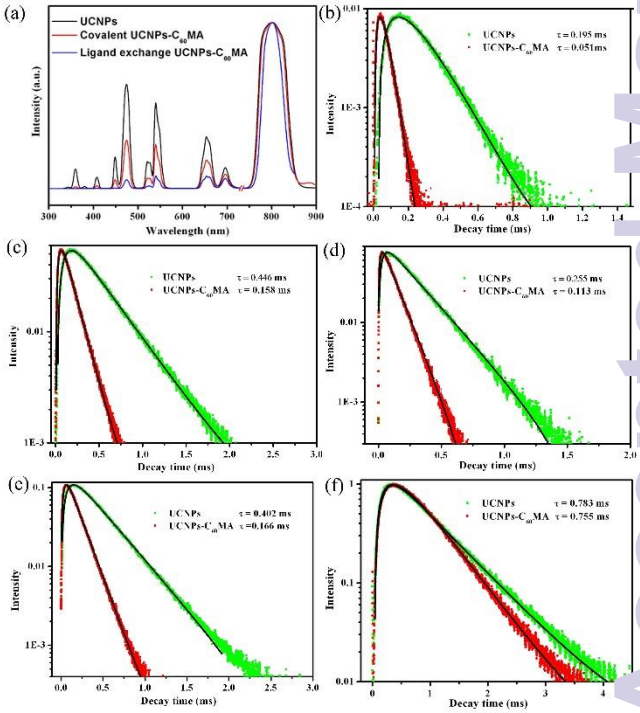

Fig. 2. (a) UCL spectra of UCNPs (black), covalent conjugated UCNPs-C_{60}MA (red) and ligand exchange assembled UCNPs-C_{60}MA (blue) nanophotosensitizer (normalized by the intensity at 808 nm, the range from 300 to 730 nm was magnified by a factor of 10). (b-f) Luminescence decay curves of upconversion emissions monitored (b) at 450 nm, (c) at 475 nm, (d) at 540 nm, (e) at 650 nm, (f) at 80 nm for UCNPs (in green) and ligand exchange assembled UCNPs-C_{60}MA (red). Best fitting curves are also shown as a black solid line.

As aforementioned, the broad absorption spectrum of C_{60}MA overlapped well with the multicolor upconversion luminescence bands (360, 407, 450, 475, 540, 650 and 696 nm) of $NaYF_4$: Yb^{3+}, Er^{3+}/$NaYF_4$: Yb^{3+}, Tm^{3+} (Fig. 1c). Both steady-state upconversion luminescence (UCL) spectra and the luminescence decay kinetics evidenced the energy transfer from UCNPs to C_{60}MA. The UCL spectrum in Fig. 1d was significantly quenched in UV-VIS range by C_{60}MA. The FRET efficiency, as determined from the UCL quench as $E = (I_0 - I_1)/I_0$, where I_0 and I_1 are the emission intensities of UCNPs and UCNPs-C_{60}MA NPS, was 99.7% at 360 nm, 98.3% at 407

98.7% at 450 nm, 92.7% at 475 nm, 88.2% at 540 nm, 76.2% at 650 nm and 52.3% at 696 nm respectively. The energy transfer efficiency of covalently assembled UCNPs-C_{60}MA NPS was also measured, as shown in Fig. 2a and Table S1. After comparison it can be concluded that ligand-exchange strategy is better than covalent bonding strategy in reaching a high energy transfer efficiency, and the former is approximately 1.44 times of the latter. Such high energy transfer efficiency was ascribed to the robust ligand-exchange binding between C_{60}MA and UCNPs, which improves the stability of the nanoconjugate and shortens the energy transfer distance. On the other hand, the fullerene itself displays advantages over normal fluorescent quenchers and FRET systems in biological application, with no intrinsic fluorescence emission and the ability to quench a very broad spectrum of phosphors.[31, 32]

The energy transfer process was further studied by the temporal behavior of UCL of both UCNPs and ligand-exchange assembled UCNPs-C_{60}MA NPS recorded at 450, 475, 540, 650 and 808 nm (Fig. 2b-f). In all cases, the decay curves could be well fitted with a bi-exponential function. In the presence of C_{60}MA, however, the average decay time decreases from 195µs to 51µs for 450nm, from 446µs to 158µs for 475nm, from 255µs to 113µs for 540nm and from 402µs to 166µs for 650nm, respectively. The significantly shortening of the UCL kinetics is consistent with the efficient energy transfer obtained from the steady-state UCL quenching. The average decay time at 808 nm shows hardly any change because of the poor absorption of C_{60}MA in NIR region. The FRET efficiencies, calculated based on the change of temporal behavior (Table S2), show efficiencies of 72.8% at 450 nm, 63.1% at 475 nm, 56.3% at 540 nm and 50.8% at 650 nm, which are a little less comparing with the values determined from steady-state UCL spectra (98.7% at 450 nm, 92.7% at 475 nm, 88.2% at 540 nm, 76.2% at 650 nm). This is mainly because that with the increase of PS loading amounts, although most of them are closely attached to the surface of the UCNPs, the re-absorption process becomes inevitable due to the strong quenching ability of C_{60}MA.[35] Both re-absorption and FRET contributed to the luminescence quench. However, the re-absorption does not affect the temporal behavior of UCNPs, the shortening of the UCL lifetimes reflects specifically the FRET process. The efficient multiplexed FRET from UCNPs to C_{60}MA ensured high $^1O_2$ generation.

Another motivation of designing the UCNPs-C_{60}MA NPS was the high $^1O_2$ production yield of C_{60} derivatives, which has been proved to be even better than traditional photosensitizers. In order to assess the $^1O_2$ generation of UCNPs-C_{60}MA NPS, fluoresceinyl cypridina luciferin analogue (FCLA), which can be oxidized by $^1O_2$, leading to an increase of its fluorescence around 524 nm, was used as a $^1O_2$ indicator.[36] Fig. S7 shows the fluorescence spectra of FCLA for ligand exchange and covalently conjugated UCNPs-C_{60}MA NPS, respectively. The corresponding fluorescence intensity changes at 524 nm are depicted in Fig. 3a. The slopes of the curves represent the efficiency of singlet oxygen generation, the higher slope of ligand exchange assembled UCNPs-C_{60}MA NPS indicates distinctly its higher $^1O_2$ yield. It should be noted that the ligand exchange assembled UCNPs-C_{60}MA NPS results in twice the amount of C_{60}MA loaded compared to the covalent route. However, the generation of reactive oxygen seems less than this factor. This is mainly because that various factors may affect the $^1O_2$ production, including, among others, the energy transferred from the nanoparticle to the C_{60}MA, the loading capacity of the photosensitizers, oxygen concentration of the area, and the triplet state life time of photosensitizer. The location of the photosensitizers is also critical since the energy transfer depends severely on the distance between the energy donor and acceptor. Therefore, the generation of reactive oxygen is not a simple linear process with regard to the loading capacity of photosensitizer.

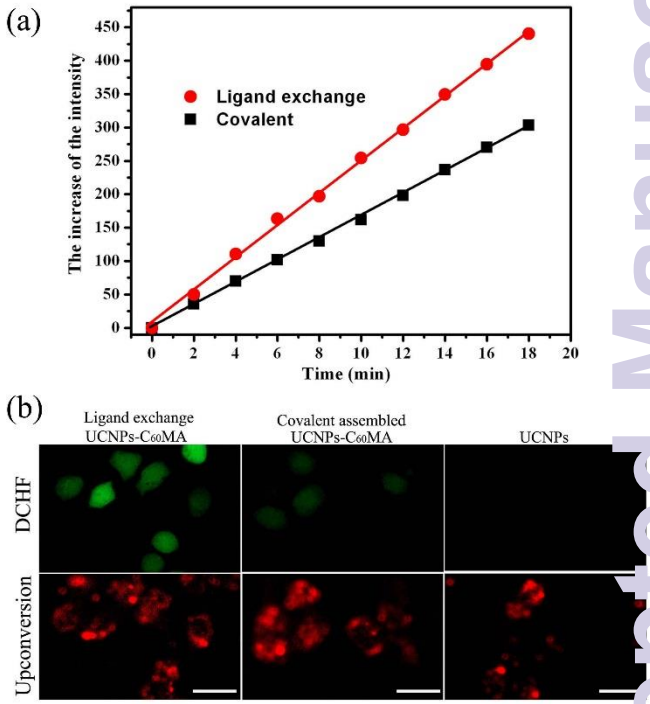

Fig. 3. (a) The increase in luminescence intensity of FCLA at 524 nm as a function of the exposure time under 980nm irradiation. (b) Detection of intracellular reactive oxygen production by DCFH-DA staining in Hela cells incubated with ligand exchange assembled UCNPs-C_{60}MA NPS (left), covalent conjugated UCNPs-C_{60}MA (middle), and void UCNPs (right). Scale bar, 20 µm.

We also examined the production of $^1O_2$ from the NPS in live cells using 2,7-dichlorfluorescein-diacetate (DCFH-DA), as a fluorogenic marker for $^1O_2$. DCFH-DA distributes in live cells and, in the presence of $^1O_2$, was oxidized to emit bright green fluorescence. We irradiated Hela cells labeled with ligand exchange and covalently conjugated UCNPs-C_{60}MA NPS under the same 980 nm light dosage (0.39W/cm^2 for 5min), respectively. The resulting oxidatively stressed cells showed green fluorescence as can be seen in Fig. 3b, indicating an increase in $^1O_2$, whereas control cells treated just with UCNPs showed negligible fluorescence. Notably, the green fluorescence of cells treated with ligand exchange assembled NPS was more intense than that of covalently conjugated ones, which further confirmed the strong $^1O_2$ generation and the superiority of ligand exchange strategy.

3.3. In Vitro cancer cell uptaking and photodynamic killing

With the $^1O_2$ generation of the UCNPs-C_{60}MA NPS having been demonstrated, we have studied the targeting cellular uptake of UCNPs-C_{60}MA NPS using HeLa cells. To achieve tumor targeting

property, folic acid (FA) was attached to PEG-b-PCL functionalized UCNPs-C_{60}MA NPS.[37,38] The loading capacity of folic acid reached to 5.1% (w/w) (see experiment section). Fig. S8 shows the target staining of the UCNPs-C_{60}MA/FA NPS in HeLa cells (FR-positive)[15] and the control result in human alveolar adenocarcinoma (A549) cells (FR-negative).[22] The UCL was collected at 808 nm - a wavelength that lies in the minimal absorption range and enables high-contrast optical imaging and high treatment depth.[39] The nanocomposites were mainly located inside the cells (Fig. S8, left), illustrating the specific targeting of the NPS. While for A549 cells, which are poor in expressing the folate receptor, few UCNPs-C_{60}MA/FA NPS were stained (Fig. S8, right).

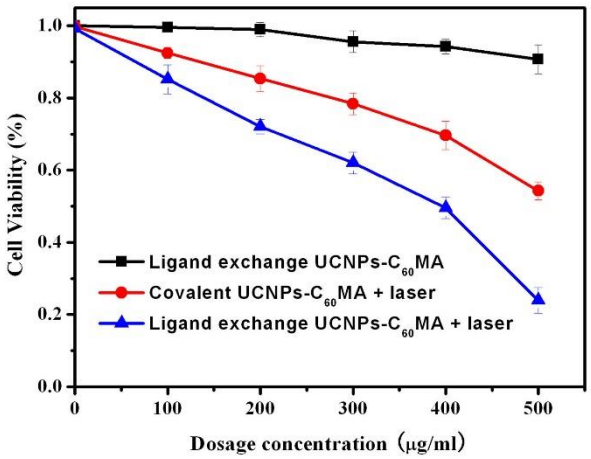

Fig. 4. The photodynamic capabilities of covalent conjugated UCNPs-C_{60}MA (red; 980 light dosage: 1.37 W/cm^2 for 10min) and ligand exchange assembled UCNPs-C_{60}MA NPS (blue; 980 light dosage: 0.39 W/cm^2 for 10min).

The NIR light triggered photodynamic therapy of cancer cells by UCNPs-C_{60}MA/FA NPS was firstly studied *in vitro*. Hela cells were incubated with NPS at different concentrations. The cell viability as determined from the MTT assay is shown in Fig. 4. The dark toxicity became non-negligible only when the concentration was higher than 500 μg/mL (100 μL), at which point the cell viability went down to nearly 90%. When HeLa cells were exposed to 980nm NIR light at a relatively low density of 0.39 W/cm^2 for 10 min, the cells' decline could be observed. The decline was getting faster with the increase of the NPS concentration. It was also evidenced from Fig. S9 that most of the cells treated with 100 μg/mL (100 μL) NPS kept their healthy spindle morphologies upon light exposure. When the dosage was increased to 300 μg/mL (100 μL), majority of them were dead. Increasing further the dosage to 500 μg/mL (100 μL), almost all of the cells shrank and lost their normal morphology. Photodynamic therapy using the covalent conjugated UCNPs-C_{60}MA model was also tested under similar conditions for comparison, which was obviously less efficient, emphasizing the superior cancer cell killing ability of the designed ligand exchange UCNPs-C_{60}MA photosensitizing nanoplatform. Besides the human Hela cell, the mouse Hepa1-6 cell line was chosen for *in vitro* test (Fig. S10), also demonstrating an efficient PDT effect.

3.4. In Vivo Tumor-targeting and Therapeutic efficacy

The *in vivo* bio-distribution and tumor targeting ability of the UCNPs-C_{60}MA/FA NPS were tracked in mice bearing Hepa1-6 tumors (FR-positive),[40] which were administrated with NPS and imaged at different times (Fig. 5). Two hours after *in vivo* tail vein injection, 808 nm luminescence emitted from NPS was distinctly visualized in the superficial vasculature of the mouse. Subsequently, as blood circulated, the NPSs were seen to gradually distribute and deposit inside different organs. Significant tumor uptake was clearly visible in mice treated with NPS after 2 h post-injection (pi). By 24 h pi, the maximal tumor luminescence was attained and persisted for more than 48h pi. The NPS exhibited prominent distribution in tumor, liver and bladder after 48h pi. By 72h pi, the NPSs were cleared from the circulation and the luminescence signals in the liver decreased, but were still visible. As indicated by the luminescence signal, NPS remained visible in the circulation, even after 72h pi (Fig. 5a and 5b). The spectral unmixed, high contrast images (Fig. 5c) clearly demonstrate the feasibility to image and spectrally distinguish the characteristic emission of the NPS (shown as red). A scan in the range of 700-820nm showed an intense luminescence peaking at ~800nm, strongly evidenced the 808nm NIR imaging (Fig. 5e). The high contrast between the background and the luminescence signal from NPS came from NIR to NIR upconversion luminescence imaging.

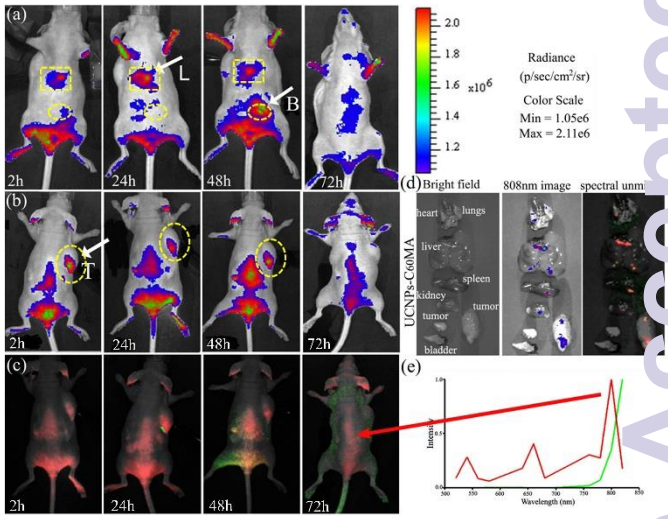

Fig. 5. *In vivo* tumor-targeting and biodistribution of UCNPs-C_{60}MA/FA nanophotosensitizer. Fluorescence images of nude mouse bearing Hepal-6 tumor. Images were taken at different time points after iv injection of UCNPs-C_{60}MA nanophotosensitizer (a) ventral images; (b) dorsal images and (c) dorsal spectral unmixed images. Arrows mark the location of the tumor (T), liver (L), and bladder (B). (d) Fluorescence images of isolated organs separated from mice in different groups at 72h post-injection. (e) PL spectra corresponding to the spectrally unmixed components of the multispectral image, the red color indicates 808nm emission from UCNPs and the green color is autofluorescence.

To further support the tumor selective targeting of the designed nanophotosensitizer, results of mice bearing tumors are provided in Fig. S11 which were administrated with UCNPs-C_{60}MA/FA or UCNPs-C_{60}MA and imaged at different time points. Tumor uptake in mice treated with UCNPs-C_{60}MA became visible only at 24 h post

injection as a result of enhanced permeation and retention (EPR effect) in the tumor accumulation of the NPs, whereas UCNPs-C_{60}MA/FA were already accumulated in tumor area at 2h post-injection. To confirm the *in vivo* imaging results, the *ex vivo* organ optical imaging has been performed. Fig. 5d shows *ex vivo* optical images of resected organs at 72h pi. It is obvious that relatively intensive luminescence of UCNPs-C_{60}MA/FA NPS remained mainly in the tumor, liver and kidney. However, the relative organs of uninjected mice showed no comparable luminescence (Fig. S12). The results demonstrated that major sites of luminescence seen by *ex vivo* optical imaging were in line with those in noninvasive imaging, supporting the high tumor selectivity and indicating also that the bio-distribution of the designed NPS inside organs could be sensed and imaged *in vivo*.

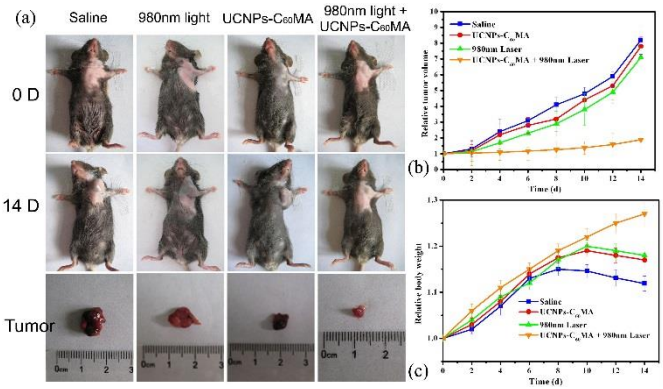

Fig. 6. (a) Representative photos of mice and tumor before and after various treatments indicated. (b) Tumor growth of mice in different treatment groups within 14 days. (c) Changes of body weight of mice in different groups during PDT. n = 6 per group; $p < 0.05$; Error bars represent standard errors of the mean.

With the tumor uptake of the nanoplatform having been demonstrated, the *in vivo* PDT treatment by UCNPs-C_{60}MA NPS was explored in Hepa1-6 tumor-bearing C57/6J mice, which have immune system and can be raised in natural environment. Moreover, such kind of mice is similar to human tumor patients in pathological change. Therefore they are appropriate for PDT study. The Hepa1-6 tumor model was established by subcutaneously inoculating Hepa1-6 cells (3×10^6) into the upper axillary fossa in the mice (n = 6). The tumors were irradiated with a 980 nm laser light at 0.39 W/cm^2 for 15 min, namely the 980 nm irradiation dosage was 351 J/cm^2. It is worth noting that the NIR laser power used here (0.39 W/cm^2) is far below the conservative limits set for human skin exposure to 980 nm light (0.72 W/cm^2).[17] We found no skin burn scars caused by the generation of excessive local heating ascribed to the NIR laser irradiation in any of the mice (Fig. 6a). After treatment, the tumors were isolated from the different groups of mice and weighed. As can be seen from Fig. 6a and 6b**,** the mice treated with saline, just 980 nm light irradiation or NPS without light irradiation did not show any therapeutic effect. While the mice received injection of the NPS with 980 nm NIR light irradiation shows very high tumor inhibition ratio (78.5%). Body weight change can also reflect the health condition of the treated mice. As shown in Fig. 6c, the body weight of mice in the control group began to decrease from day 8 post-treatment, which indicates the living quality of the mice was effected by the tumor burden. For the PDT treated group, their body weight gradually increased during 14 days, demonstrating that PDT treatment based on UCNPs-C_{60}MA NPS could effectively improve the survival quality of mice and prolong their lifetime. It should be emphasized the lowest irradiation power used for the PDT based on UCNPs studies to-date was 360 J/cm^2 with the nanophotosensitizer dosage of 50 mg/kg.[42] However, the situation was greatly improved in our study that under the irradiation power of 351 J/cm^2 and drug dosage of only 17 mg/kg, the tumor inhibition ratio can reach up to 78.5% by using the designed nanophotosensitizer, evidencing the efficient energy transfer benefited from the ligand-exchange construction.

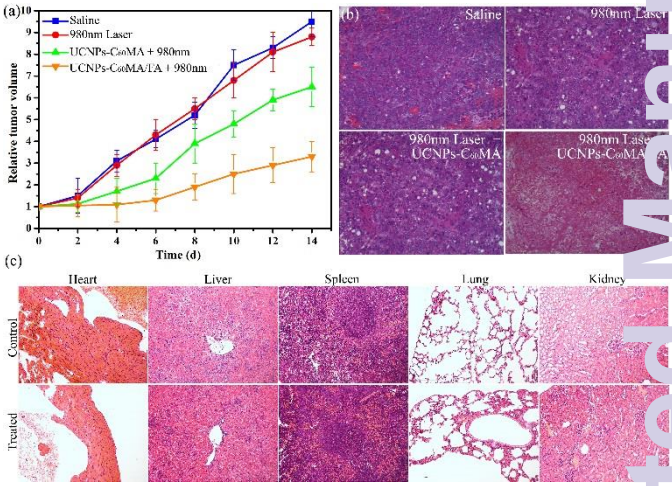

Fig. 7. (a) Tumor growth of mice in different treatment groups within 14 days. n = 6 per group; $p < 0.05$; Error bars represent standard errors of the mean. H&E stained images of (b) tumor, (c) heart, liver, spleen, lung, kidney collected from different groups.

We further extended the study to examine the targeted PDT efficacy of UCNPs-C_{60}MA/FA NPS. The experiment details were the same as we did in intratumorally injection with the except that UCNPs-C_{60}MA/FA or UCNPs-C_{60}MA nanophotosensitizers were intravenously injected into the mice bearing Hepa1-6 tumors. It should be noted that the light spot we used could only cover the tumor area. By selectively irradiating only the disease site, little or no damage is incurred to surrounding healthy tissues. Therefore, for *in vivo* targeted PDT, we need to get the information from in vivo imaging like how long the nanophotosensitizer could accumulate and remain in the tumor after iv injection. As indicated in Fig. 5b, the concentration of the nanophotosensitizer in the tumor can be reflected by the intensity of NIR luminescence signal. Significant tumor uptake was clearly visible in mice treated with nanophotosensitizer after 2h post-injection (pi) and persisted for more than 48h pi. Under the guidance of this information, after 2h pi, the tumors were irradiated with a 980 nm laser light at 0.39 W/cm^2 for 15 min every day. In addition, the nanophotosensitizer have to be intravenously injected every 3 days to guarantee that the nanophotosensitizers exist in the tumor. We found no such significant antitumor effect in mice treated with saline or just under 980 nm light irradiation. While the mice received intravenous injection of UCNPs-C_{60}MA/FA NPS shows a relative higher tumor inhibition ratio (66.3%) than that of the control mice treated with folic acid unmodified UCNPs-C_{60}MA NPS (33.5%), indicating that

active targeting by modifying the surface of the NPS with cancer-specific targeting agents has an important role in improving the therapeutic efficacy for a desirable PDT outcome (Fig. 7a). The histological analysis on tumor, heart, liver, spleen, lung, and kidney was carried out in different treatment groups after 14 days of post-treatment. It can be clearly observed in Fig. 7b that the morphology, size and staining of the tumor cells in saline group are at variance, and mitotic figures are seen in most nuclei. It is the similar situation for the 980 nm laser group. However, markedly increased apoptotic and necrotic tumor cells were observed in targeted PDT treatment groups. Histological analysis shown in Fig. 7c reveals no pathological changes in the heart, lung, kidney, liver or spleen. Hepatocytes in the liver samples were found normal. No pulmonary fibrosis was detected in the lung samples. The glomerulus structure in the kidney section was observed clearly. Necrosis was not found in any of the histological samples analyzed. These results clearly demonstrate the targeted PDT efficacy of the as-designed UCNPs-C_{60}MA/FA NPS. There are three main mechanisms involved in this PDT mediated tumour destruction.[41] In the first case, the singlet oxygen that is generated by PDT can kill tumor cells directly. PDT also damages the tumor-associated vasculature, leading to tumor infarction. Finally, PDT can activate an immune response against tumor cells. Notably, the tumor inhibition ratio of intravenous injection (66.3%) was smaller than that of intratumoral injection (78.5%), because intravenous injection might face physiological barriers, such as spatially and temporally heterogeneous blood flow, high vascular permeability. Even in intratumoral injection, the tumors were not completely regressed as a result of injection of UCNPs-C_{60}MA NPS and irradiation, as is expected in an ideal scenario of cancer therapy. Further optimizations of the experimental conditions are still required to exploit the full potential of these NPSs as a PDT drug to be used in the clinic. These may include optimization of UCNP synthesis for even brighter UCL emission, further improvement of the $^1O_2$ generation or the dose of NPS injected.

4. Conclusions

In this work, we have proposed a feasible *in vivo* 808nm image-guided PDT based on an effective upconversion-C_{60} nanoplatform constructed via ligand-exchange strategy, which could greatly improve the FRET efficiency between donor and acceptor by shortening the energy transfer distance. Ascribing to the optimized FRET efficiency, and the monomalonic fullerene (C_{60}MA) PS molecules which exhibit nearly 100% $^1O_2$ yield, high $^1O_2$ production yield was achieved to such that NIR illumination power as low as 351 J/cm^2 were sufficient to perform simultaneous imaging and PDT. Based on the results of NIR imaging, the designed nanoplatform was demonstrated to exhibit high noninvasive detection sensitivity, favorable bio-distribution and enhanced tumor-selectivity. Tests performed on *in vivo* PDT evidenced its remarkable therapeutic efficacy. These results indicate that the upconversion-C_{60} NPS is a promising PDT agent for NIR to NIR simultaneous diagnosis and therapy.

Acknowledgements

This work was financially supported by NSF of China (11174277, 11374297, 11474278, 61275202, 21304084), Joint research program between CAS of China and KNAW of the Netherlan the IOP program of The Netherlands, and John van Geun foundation.

Notes and references

1 A. P. Castano, P. Mroz, M. R. Hamblin, *Nat Rev Cancer* 2006, **6**, 535.
2 L. R. Braathen, R. M. Szeimies, N. B. Seguin, B. Bissonnette, H Foley, D. Pariser, R. Roelandts, A. M. Wennberg, C. A Morton, *J Am Acad Dermatol* 2007, **56**, 125.
3 P. Rai, S. Mallidi, X. Zheng, R. Rahmanzadeh, Y. Mir, S. Elrington, A. Khurshid, T. Hasan, *Adv Drug Delivery Rev* 201 **62**, 1094.
4 J. P. Celli, B. Q. Spring, I. Rizvi, C. L. Evans, K. S. Samkoe, S Verma, B. V. Pogue, T. Hasan, *Chem Rev* 2010, **12**, 2795.
5 N. J. J. Johnson, A. Korinek, C. H. Dong, F. C.J. M. Van Verggel, *J. Am. Chem. Soc.* 2012, **134**, 11068.
6 F. Zhang, Y. F. Shi, G. B. Braun, Y. C. Zhang, X. H. Sun, N. O Reich, D. Y. Zhao, G. D. Stucky, *J Am Chem Soc* 2010, 1 2850-51.
7 H. S. Mader, S. P. Kele, M. Saleh, O. S. Wofbeis, *Curr Opin Chem Biol* 2010, **14**, 582.
8 F. Wang, X. G. Liu, *Chem Soc Rev* 2009, **4**, 976.
9 M. Haase, H. Schäfer, *Angew Chem Int Ed* 2011, **50**, 5808.
10 Y. Liu, K. Ai, J. Liu, Q. Yuan, Y. He, L. H. Lu, *Angew Chem Int E* 2011, **51**, 1437.
11 P. Zhang, W. Steelant, M. Kumar, M. Scholfield, *J Am Che Soc* 2007, **129**, 4526.
12 K. C. Dev, Y. Zhang, *Nanomedicine* 2008, **3**, 73.
13 H. Qian, H. Guo, P. Ho, R. Mahendran, Y. Zhang, *Small* 2009, **5**, 2285-90.
14 J. N. Shan, S. J. Budijono, G. Hu, N. Yao, Y. Kang, Y. Ju, P. K. Prud'homme, *Adv Funct Mater* 2011, **21**, 2488.
15 C. Wang, H. Tao, L. Cheng, Z. Liu, *Biomaterials* 2011, **32**, 614.
16 M. E. Lim, Y. L. Lee, Y. Zhang, J. J. H. Chu, *Biomaterials* 2012 **33**, 1912.
17 N. M. Idris, M. K. Gnanasammandhanl, J. Zhang, P. C. Ho, R. Mahendran, Y. Zhang, *Nature Medicine* 2012, **18**, 1580.
18 X. F. Qiao, J. C. Zhou, J. W. Xiao, Y. F. Wang, L. D. Sun, C. Yan, Nanoscale 2012, **4**, 4611.
19 K. Liu, X. M. Liu, Q. H. Zeng, Y. L. Zhang, L. P. Tu, T. Liu, X. G. Kong, Y. Wang, F. Cao, S. A. Lambrechts, H. Zhang, *ACS Nan* 2012, **6**, 4054.
20 Y. I. Park, H. M. Kim, J. H. Kim, K. C. Moon, B. Yoo, K. T. Lee, N Lee, Y. Choi, W. Park, D. Ling, *Adv Mater* 2012, **24**, 5755.
21 S. Cui, H. Chen, H. Zhu, J. Tian, Z. Qian, S. Achilefu, Y. Q. Gu, *Mater Chem* 2012, **22**, 4861.
22 S. S. Cui, D. Y. Yin, Y. Q. Chen, Y. F. Di, H. Y. Chen, Y. X. Ma, S Achilefu, Y. Q. Gu, *ACS nano* 2013, **7**, 676.
23 H. Guo, H. Qian, N. M. Idris, Y. Zhang, *nanomedicine* 2009, **6** 486.
24 F. Wang, D. Banerjee, Y. S. Liu, X. Y. Chen, X. G. Liu, *Analyst* 2010, **135**, 1839.
25 D. M. Guldi, M. Prato, *Acc Chem Res* 2000, **33**, 695.
26 S. Fukuzumi, T. Suenobu, M. Patz, T. Hirasaka, S. Ito, M Fujitsuka, *J Am Chem Soc* 1998, **120**, 8060.
27 H. Fueno, Y. Takenaka, K. Tanaka, *Optics and Spectroscopy* 2011, **111**, 248.
28 J. W. Arbogast, C. S. Foote, *J Am Chem Soc* 1991, **113**, 8886.
29 T. Nagano, K. Arakane, A. Ryu, T. Masuanga, K. Shinmoto, S Mashiko, M. Hirobe, *Chem Pharm Bull* 1994, **42**, 2291.

30 J. W. Arbogast, A. P. Darmanyan, C. S. Foote, Y. Rubin, F. N. Diederich, M. M. Alvarez, S. J. Anz, R. L. Whetten, *J Phys Chem* 1991, **95**, 11.
31 K. D. Pickering, R. Wiesner, *Environ Sci Technol* 2005, 39, 1359.
32 T. Da Ros, M. Prato, *Chem Commun* 1999, 663.
33 B. Ungun, R. K. Prud'homme, S. J. Budijono, J. N. Shan, S. F. Lim, Y. G. Ju, R. Austin, *Opt Express* 2009, **17**, 80.
34 X. M. Liu, M. Zheng, X. K. Kong, Y. L. Zhang, Q. H. Zeng, Z. C. Sun, W. J. Buma, H. Zhang, *Chem Commun* 2013, **49**, 3224.
35 S. M. Saleh, R. Ali, T. Hirsch, O. S. Wolfbeis, *J Nanopart Res* 2011, **13**, 4603.
36 A. G. Zhou, Y. C. Wei, B. Y. Wu, Q. Chen, D. Xing, *Mol Pharmacetics* 2012, **9**, 1580.
37 S. Chen, X. Z. Zhang, S. X. Cheng, R. X. Zhou, Z. W. Gu, *Biomacromolucules* 2008, **9**, 2578.
38 L. M. Yao, J. Zhou, J. L. Liu, W. Feng, F. Y. Li, *Adv Funct Mater* 2012, **22**, 2667.
39 M. Nyk, R. Kumar, T. Y. Ohulchanskyy, E. J. Bergey, P. N. Prasad, *Nano Lett* 2008, **8**, 3834.
40 A. M. Nour, D. Ringot, J. L. Gueant, A. Chango, *Carcinogenesis* 2007, **28**, 2291.
41 D. E. Dolmans, D. Fukumura, R. K. Jain, *Nat Rev Cancer* 2003, **3**, 380.
42 N. M. Idris, M. K. G. Jayakumar, A. Bansal, Y. Zhang, *Chem Sov Rev* 2015, **44**, 1449.